A&A 536, A29 (2011)
DOI: 10.1051/0004-6361/201117787

Astronomy & Astrophysics

VLT adaptive optics search for luminous substructures in the lens galaxy towards SDSS J0924+0219⋆

C. Faure[1], D. Sluse[2,3], N. Cantale[1], M. Tewes[1], F. Courbin[1], P. Durrer[1], and G. Meylan[1]

[1] Laboratoire d'astrophysique, Ecole Polytechnique Fédérale de Lausanne (EPFL), Observatoire de Sauverny, 1290 Versoix, Switzerland
e-mail: cecile.faure@epfl.ch
[2] Astronomisches Rechen-Institut am Zentrum für Astronomie der Universität Heidelberg, Mönchhofstrasse 12-14, 69120 Heidelberg, Germany
[3] Argelander-Institut für Astronomie, Auf dem Hügel 71, 53121 Bonn, Germany

Received 29 July 2011 / Accepted 29 September 2011

ABSTRACT

The anomalous flux ratios between quasar images are suspected of being caused by substructures in lens galaxies. We present new deep and high-resolution *H* and *K*s imaging of the strongly lensed quasar SDSS J0924+0219 obtained using the ESO VLT with adaptive optics and the laser guide star system. SDSS J0924+0219 is particularly interesting because the observed flux ratio between the quasar images vastly disagree with the predictions from smooth mass models. With our adaptive optics observations we find a luminous object, Object L, located ~0.3″ to the north of the lens galaxy, but we show that it cannot be responsible for the anomalous flux ratios. Object L as well as a luminous extension of the lens galaxy to the south are seen in the archival HST/ACS image in the *F814W* filter. This suggests that Object L is part of a bar in the lens galaxy, as also supported by the presence of a significant disk component in the light profile of the lens galaxy. Finally, we find no evidence of any other luminous substructure that may explain the quasar images flux ratios. However, owing to the persistence of the flux ratio anomaly over time (~7 years), a combination of microlensing and millilensing is the favorite explanation for the observations.

Key words. gravitational lensing: strong – quasars: individual: SDSS J092455.87+021924.9

1. Introduction

Strong gravitational lensing is now part of the standard toolbox of the astrophysicist. It consists in a powerful test for cosmological models (e.g. Barnabè et al. 2011; Suyu et al. 2010; Coe & Moustakas 2009; Fedeli et al. 2008; Fedeli & Bartelmann 2007) and allows us to study the distribution of luminous and dark matter in galaxies, as well as the evolution of their properties with redshift (e.g. Ruff et al. 2011; Faure et al. 2011; Tortora et al. 2010; Auger et al. 2010; Koopmans et al. 2006).

Such studies require a model for the total projected potential well of lensing galaxies, which is often described as a smooth 2D elliptical profile, with or without contribution of intervening objects along the line of sight. However, the increasing accuracy of the observational constraints provided by high-resolution imaging has quickly shown the limitations of such simple models. In quadruply imaged quasars, smooth models are often unable to account simultaneously for the milliarcsec astrometry and for the near- and mid-IR flux ratios of the quasar images (Vegetti et al. 2010a; Chantry et al. 2010; Yoo et al. 2005; Biggs et al. 2004; Kochanek & Dalal 2004; Keeton et al. 2003; Metcalf & Zhao 2002; Koopmans et al. 2002; Mao & Schneider 1998).

The reason for the observed discrepancies between the model predictions and the measurements may be the presence of substructures in the halo of lensing galaxies. Such small deviations in the smooth potential might significantly affect the predicted flux ratios while barely changing the astrometry of the quasar images. This is especially true when a quasar image is a saddle point of the arrival time surface (Schechter & Wambsganss 2002). Strong lensing therefore offers a sensitive way to indirectly detect and weight substructures in galaxy halos, whether luminous or not (e.g. Vegetti et al. 2010b; Suyu & Halkola 2010; More et al. 2009; McKean et al. 2007).

In the present work, we have searched for substructures in the halo of the lens galaxy towards the quadruply imaged quasar with the most anomalous flux ratios, SDSS J0924+0219 (Inada et al. 2003), at $z_{\rm quasar} = 1.524$, discovered in the Sloan Digital Sky Survey (SDSS, York et al. 2000). *Hubble* Space Telescope (HST) spectra of the system reveal that one of the quasar images, labeled D in Inada et al. (2003; see also Fig. 2), is extremely faint (Keeton et al. 2006). It is also a saddle point in the arrival time surface, hence making it more likely to be demagnified owing to micro- and millilensing (Schechter & Wambsganss 2002). The microlensing hypothesis provides a satisfying explanation for the observed flux ratio anomaly (Bate et al. 2011; Mediavilla et al. 2009; Morgan et al. 2006; Keeton et al. 2006). However, this flux anomaly lasts for at least seven years, which is significantly more than the expected duration of microlensing fluctuations in this lens (0.39 years), and longer than the duration averaged over a sample of 87 lenses, i.e., 7.3 months (Mosquera & Kochanek 2011). It is therefore conceivable that not only does stellar-microlensing take place in this system but also that a more

⋆ Based on observations obtained with the ESO VLT at Paranal observatory (Prog ID 084.A-0762(A); PI: Meylan). Also based in part on observations made with the NASA/ESA *Hubble* Space Telescope, obtained at the Space Telescope Science Institute, which is operated by the Association of Universities for Research in Astronomy, Inc., under NASA contract NAS 5-26555. These observations are associated with the CASTLES (Cfa-Arizona Space Telescope LEns Survey) survey (ID: 9744, PI: C. S. Kochanek).

extended/massive substructure also contributes to the observed anomaly. A deep spectrum of the lens galaxy was obtained with the ESO Very Large Telescope (VLT) and the FORS1 instrument (Eigenbrod et al. 2006), leading to $z_{\rm lens} = 0.394 \pm 0.001$ from stellar absorption lines. In addition Eigenbrod et al. (2006) notice numerous elongated features within and around the Einstein ring in the HST images. This observation leads them to conclude that the lensed source may be double.

To further investigate the nature of these features and to look for possible faint and small satellites in the lensing galaxy, we conduct deep adaptive optics (AO) imaging observations of SDSS J0924+0219 with the VLT. The paper is organized as follows. In Sect. 2, we present the VLT AO observations and the HST dataset. In Sect. 3 we detail our findings of a luminous substructure in the AO images. In Sect. 4, we show that the substructure is also present in the optical, from HST/ACS observations. In Sect. 5, we discuss the possible nature of the substructure. Finally, we present our conclusions in Sect. 6.

Throughout this paper, the WMAP5 ΛCDM cosmology is assumed ($\Omega_{\rm m} = 0.258$, $\Omega_\Lambda = 0.742$, $H_0 = 72$ km s^{-1} Mpc^{-1}). All magnitudes are in the AB system.

2. The datasets

2.1. Adaptive optics imaging with the VLT and NACO

We observed SDSS J0924+0219 with the near-infrared camera CONICA, which is mounted on the AO system NAOS, NACO for short, installed at the Nasmyth B focus of the VLT-UT4 at the ESO Paranal Observatory, Chile. Our observations were obtained on 2010 March 12 and 14 (H- and Ks-bands) and on 2009 December 14 (Ks-band), using the laser guide star facility. The star U0900-06393922 ($V = 16.5$ mag), located 47″ away from our target, was used to correct for "tip-tilt". The S27 CONICA camera has a pixel size of $x = 27.053 \pm 0.019$ mas and a field-of-view of 28″ on a side. A total of 30 (41) exposures of 3×60 s (NDIT × DIT) was obtained in the Ks- (H-) band, with airmasses in the range sec(z) = 1.1−1.3. The weather conditions were photometric.

The reduction procedure follows the steps exposed in Sluse et al. (2008) i.e., we first subtract dark frames to all the near-IR science images and we apply standard flat-fielding. We use twilight flat-fields obtained at most four days before the observations. We check for the temporal stability of these calibrations: flat-fields obtained four days apart are undistinguishable while flat-fields obtained four months apart show differences <2%.

The frames are divided in subsets of continuous observations. Each frame is sky-subtracted using the `xdimsum` IRAF[1] package. Each image is visually inspected to exclude data with unreliable sky subtraction, with residual cosmic rays, or with a too heavily distorted point spread function (PSF). Finally, we construct two deep images by combining 27 (28) frames in the Ks-band (H-band) using the `xnregistar` task. The total equivalent exposure time is 4860 s in the Ks filter and 5040 s in the H filter.

The PSFs of the combined images has a full width at half maximum of $FWHM \sim 0.25''$ in the H-band and $FWHM \sim 0.20''$ in the Ks-band, with a moderate ellipticity, $\epsilon \sim 0.1$. Based on the observations of standard stars on 2009 December 13 and on 2010 March 13, we derive photometric zeropoints: ZP(Ks) = 23.05 ± 0.15 mag s^{-1} and ZP(H) = 24.06 ± 0.10 mag s^{-1}. The large uncertainties on the zeropoints reflect mainly the temporal variations in the low-frequency wings of the PSF and angular anisoplanatism (see e.g. Esslinger & Edmunds 1998). Extinction corrections of 0.034 mag in the H-band and 0.043 mag in the Ks-band are used to flux-calibrate the science frames (Lombardi et al. 2011).

2.2. HST optical imaging with the ACS

Optical HST images of SDSS J0924+0219 are available from the archives (ID: 9744, PI: C. S. Kochanek). These data consist of F814W and F555W drizzled images obtained with the wide field aperture of the Advanced Camera for Surveys (ACS). The four F814W drizzled images were initially taken on 2003 November 18 and 19 with an exposure time of 574 s each. The four F555W frames were observed in 2003 November 18 with a total exposure time of 547 s each. The images have only recently been drizzled (April 2010, Koekemoer et al. 2002). The nondrizzled dataset was presented for the first time by Keeton et al. (2006) and used in Eigenbrod et al. (2006). In the following, we use the latest drizzled images directly from the archives. The pixel size in these images is 0.05″.

3. Analysis of the NACO images

Our goal with the AO images is to detect any possible faint and small satellite to the lens galaxy. Given the spatial scales involved, such satellites are hidden in the glare of the quasar images or of the lens galaxy itself. It is therefore mandatory to estimate the AO PSF properly and to subtract the light contribution of the quasar images and of the lens galaxy from the data.

3.1. PSF construction

With the small field of view of the NACO instrument, no bright star is available to measure the PSF. We therefore create a PSF using the quasar images themselves. For that purpose, we use the following iterative method.

First, we estimate a guess PSF by combining the images of the three brightest quasar images. Lets call it $\rm PSF_0$. The three quasar images are aligned and normalized to their peak intensity. $\rm PSF_0$ is built by assigning, at every pixel location, the lowest pixel value among the three quasar images. $\rm PSF_0$ is then used in `Galfit` (Peng et al. 2010, 2002) to fit and subtract the four quasar images. The resulting image obviously shows strong residuals at each quasar position. We median-combine these residuals, previously normalized and aligned. The result of this operation is then weighted by the square root of $\rm PSF_0$, and added to the latter to build $\rm PSF_1$, our next estimate of the PSF. This relatively arbitrary weighting allows the noise contamination of the pixels located far away from the PSF center to be minimized, i.e., where $\rm PSF_0$ is already a good approximation of the true PSF.

Second, we fit the galaxy light profile using a Sersic plus an exponential disk, in addition to the four quasar images. This light model is convolved by $\rm PSF_1$ during the fit. The fit of the lens galaxy is not possible in the first step of the PSF creation because the poor quality of $\rm PSF_0$ prevents `Galfit` to converge properly. We note that using an exponential disk in addition to the Sersic profile to model the lens galaxy is crucial for obtaining acceptable fits. The residual image obtained with the improved

[1] IRAF is distributed by the National Optical Astronomy Observatories, which are operated by the Association of Universities for Research in Astronomy, Inc., under cooperative agreement with the National Science Foundation.

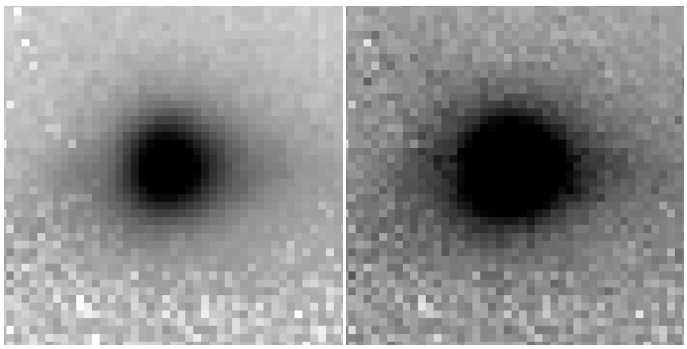

Fig. 1. PSFs created for the NACO *Ks*-band image. *Left*: zero order estimate of the PSF, i.e., PSF_0 (see text). *Right*: PSF_5, displayed here with the same gray scale as PSF_0 (logarithmic scale).

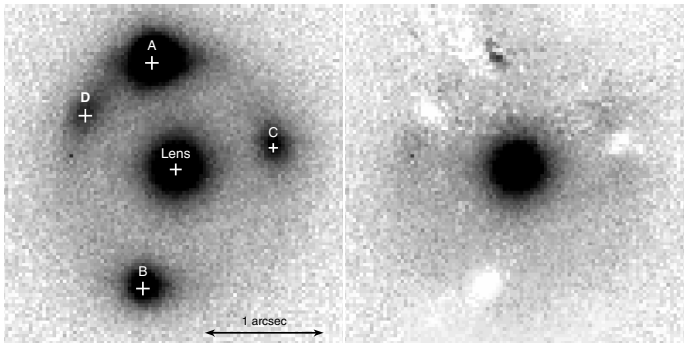

Fig. 2. NACO *Ks*-band image of SDSS J0924+0219. *Left*: combined frame, where the quasar images are labeled following Inada et al. (2003). *Right*: same image where the quasar images have been fitted using PSF_5 and subtracted using `Galfit`. The residuals at the quasar positions are negligible.

PSF and lens model is used to compute a new estimate of the PSF, which we call PSF_2.

We then repeat this second step until the residuals to the fit at the quasar positions cannot be improved anymore. A typical number of five cycles is necessary to achieve this goal. We show in Fig. 1 the PSF obtained after five iterations, for the *Ks*-band image. As mentioned in Sect. 2.1, the PSF ellipticity is $\epsilon \sim 0.1$. The apparent elongation of PSF_5 in Fig. 1 is noticeable only at large radius and is visible because of the logarithmic scale. It is also typical of the NACO PSF shape, as observed in other targets of our observational program. Figure 2, shows the *Ks*-band image after subtracting the quasar images using PSF_5. We do not observe systematic residuals under the quasar images, hence indicating that PSF_5 is reliable.

The four quasar images are located at very different positions on the Einstein ring. The quasar host galaxy therefore has very different position angles (PA) at the four quasar positions. This fortunate configuration leads to minimizing the quasar host galaxy contribution when median-averaging the residuals at each step of the PSF construction.

3.2. Quasar image fits

We do not detect any luminous object under the quasar wings. The quasar image fits include light from the ring (Fig. 2). This prevents us from accurately measuring the quasar image magnitude. Rough estimates of the magnitude differences between images A and D are $\Delta(M_D - M_A)_H \sim 3.3$ mag and $\Delta(M_D - M_A)_{Ks} \sim 2.2$ mag. They confirm the flux anomaly observed by Inada et al. (2003), even at longer wavelengths.

Table 1. Relative position of the quasar images, of the lens galaxy and of Object L to image A, as measured in the ACS/F814W deconvolved images.

	ΔRA ″	ΔDec ″
A	0.0 ± 0.001	0.0 ± 0.001
B	+0.068 ± 0.001	−1.804 ± 0.001
C	−0.957 ± 0.001	−0.701 ± 0.001
D	+0.555 ± 0.006	−0.422 ± 0.006
Lens	−0.176 ± 0.020	−0.860 ± 0.020
Obj. L	−0.15 ± 0.02	−0.52 ± 0.01

Notes. The astrometric uncertainties for the quasar images reflect the internal error of the deconvolution method. For the lens galaxy they represent the dispersion in the Sersic centroids for different acceptable fits. The quasar images are labeled as in Fig. 2.

3.3. Galaxy light profile fit and subtraction

We use `Galfit` to fit and subtract the lens galaxy from the data. We are primarily interested in a clean subtraction of the lens galaxy light within the Einstein radius. To do so, we mask the area of the Einstein ring (quasars and quasar host galaxy). The use of masks ensure that `Galfit` does not try to fit the ring as a component of the lens galaxy. However, it can be a source of inaccuracies, for example if the zone masked encompasses the galaxy effective radius.

The PSFs obtained in Sect. 3.1 are used to convolve the analytic profiles in `Galfit` in the *H* and *Ks* bands. The best fits are obtained when the lens galaxy is described as the sum of two Sersic profiles (see Fig. 3). The first one has a very shallow index, $n_1 = 0.13 \pm 0.04$ and an effective radius $R_{\rm eff,1} = 0.90 \pm 0.01''$. The second profile is much steeper, with $n_2 = 7.17 \pm 0.65$ and has a smaller effective radius, $R_{\rm eff,2} = 0.35 \pm 0.04''$. In the fits, the two profiles are separated by $\delta_{1,2} = 30 \pm 8$ mas and have $PA_{1,2} \sim -80°$ (positive north-to-east). Their ellipticity is very small, $\epsilon_{1,2} \lesssim 0.1$. The values given above are averaged over the two near-IR bands and the error bars correspond to the dispersion between those values. The agreement between the fits in the two bands is remarkable. The total magnitude of the lens galaxy is $Ks = 15.75 \pm 0.15$ mag and $H = 16.24 \pm 0.10$ mag.

According to our image decomposition with `Galfit`, the lens galaxy contains a significant disk-like structure, as suggested by the necessity of including a shallow Sersic profile in the fit. This is also suggested by earlier results in three HST bands (Eigenbrod et al. 2006). We discuss this finding further in Sect. 5. After subtracting our model of the lens galaxy (Fig. 3), we detect a faint but significant object north to the galaxy's centroid. The detection is significant both in the *H* and *Ks* filters: $Ks = 22.20 \pm 0.15$ mag, $H = 23.23 \pm 0.10$ mag, which translates in $L_V \sim 4 \pm 1 \times 10^6\ L_{\odot,V}$. This luminosity is K-corrected assuming an elliptical spectral energy distribution. We also corrected for extinction and evolution. In the following, we refer to this possible substructure of the lens as Object L.

4. Analysis of the HST images

The luminous Object L discovered in the NACO images is also visible in the ACS/F814W drizzled images. As the field of view of the ACS is much wider than that of NACO, several stars are

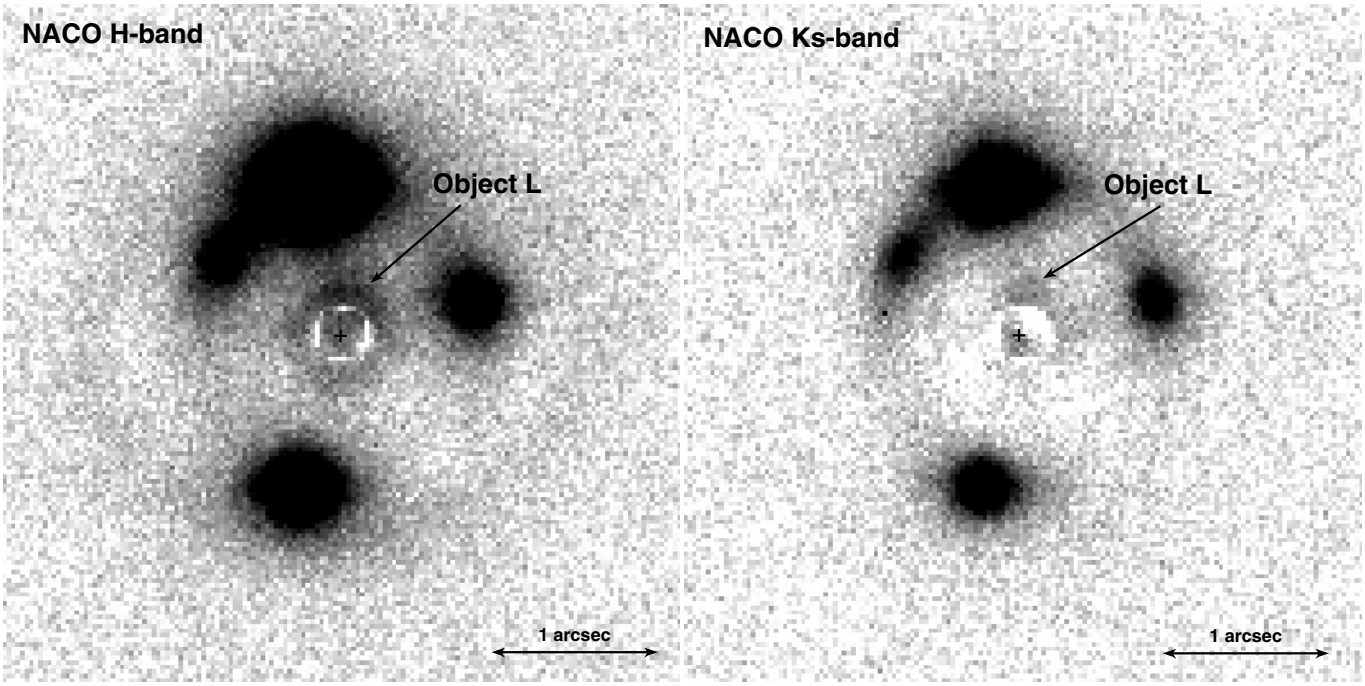

Fig. 3. VLT/NACO *H*- and *K*s-band images of SDSS J0924+0219 after subtraction of the lens galaxy with `Galfit`. North is to the top, east is to the left. The crosses indicate the fitted position of the lens. In both bands we identify a luminous residual not fitted by the Sersic profiles (Object L) located about 0.27″ to the north of the lens center.

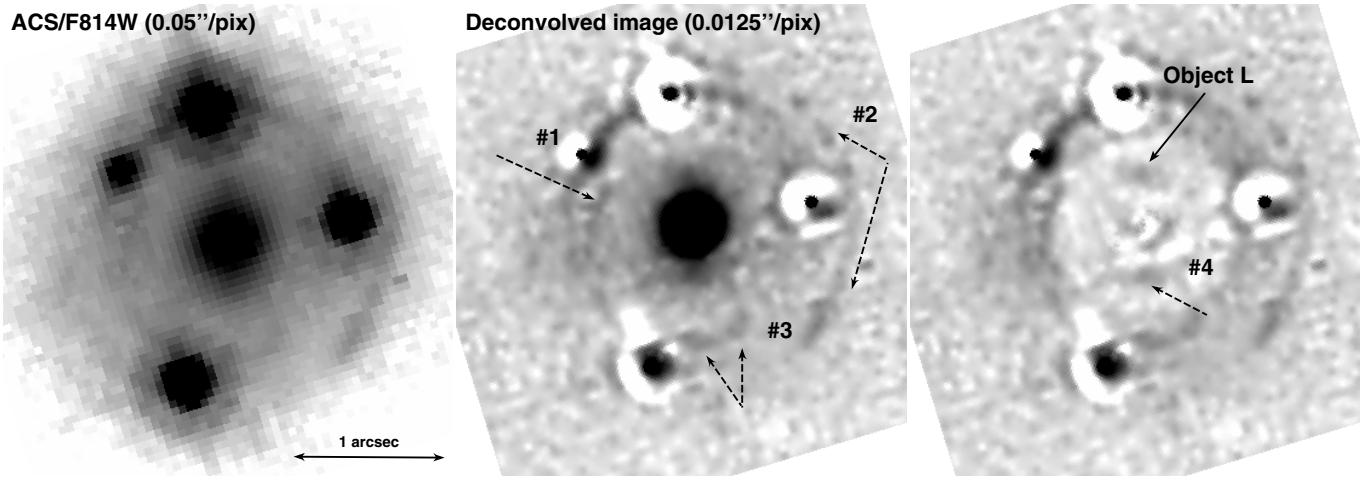

Fig. 4. HST/ACS image of SDSS J0924+0219 in the *F814W* filter. *Left*: original drizzled image obtained from the archive. *Middle*: deconvolved image. The pixel size is four times smaller than in the left panel. *Right*: deconvolved image, where the lensing galaxy profile has been fitted and removed using `Galfit`. The arc-like features #1–4 are discussed in the text. North is to the top, east to the left.

available to build a reliable PSF and to spatially deconvolve the images. To do so, we use the MCS algorithm (Magain et al. 1998). The required PSF is built using three stars located within a 2′ radius from the lens. The spatial resolution after deconvolution is $FWHM = 0.025''$. The adopted pixel size in the deconvolved data is a fourth of the original data, i.e., 0.0125″. The original F814W drizzled image and its deconvolved version are displayed in Fig. 4. We do not consider here the much shallower F555W images.

We then fit the deconvolved light profile of the lens galaxy, using a mask at the position of the ring and of the quasar images. As was the case with the VLT/NACO data, two Sersic profiles are necessary to obtain good results. The parameters of the best-fit Sersics are: $n_1 = 0.06$, $R_{\rm eff,1} = 0.43''$, $\mathrm{PA}_1 = 9°$ for the shallow profile, and $n_2 = 0.58$, $R_{\rm eff,2} = 0.14''$, $\mathrm{PA}_2 = -20°$ for the steeper profile. Their ellipticity is low ($\epsilon_{1,2} \lesssim 0.1$) and their centroid are separated by $\delta_{1,2} = 4$ mas. The total luminosity of the lens galaxy is $F814W = 19.36 \pm 0.01$ mag. The profiles are very different from those fitted in the NACO images. This might come from the different depths, wavelength ranges and stellar populations probed by the data, but also to the different masks used during the fits and to the fact that the HST image (unlike the NACO image), was preliminarily deconvolved before the use of `Galfit`. As a consequence, the photometry of the lens galaxy is possibly affected by systematics errors of several tenths of a magnitude. This result illustrates the difficulty of measuring the light profile of a lens galaxy. However, we notice that both the HST and NACO data require a disk-like component in the fit. In addition to Object L, clearly visible in the HST optical image, we show four arc-like features in

Fig. 4. Features #1, #2, and #3 have been discovered earlier in the nondrizzled image (Eigenbrod et al. 2006). They were successfully modeled as a secondary set of images at the quasar redshift. Feature #4 is identified in the ACS/F814W drizzled image for the first time. The astrometric measurements for the quasar images, the lens galaxy, and Object L are given in Table 1. We measure $F814W = 25.50 \pm 0.02$ mag for Object L, which translates into a rest frame luminosity $L_V \sim 9.4 \times 10^7\ L_{\odot,V}$ (see also Sect. 3.3).

Finally, we note that the orientation of the HST image is about −70°. Therefore, Object L cannot be a spike produced, e.g., by quasar image A or by the sharp nucleus of the lens galaxy. Removal of these spikes is in fact the main motivation for carrying out image deconvolution. In addition, Object L is present both in the space image and in the NACO images, i.e., in three independent bands with two very different instruments, making it unlikely to be an artifact in all three datasets.

5. The nature of the luminous substructure

The faint Object L seen in the VLT and HST images may be interpreted in several ways. It can be (i) a satellite of the lens galaxy, (ii) the fifth central image of the lensed quasar, (iii) the lensed image of a source unrelated to the quasar, or (iv) the brightest part of a bar in the lens galaxy. In the following, we test the different hypotheses that use simple lens modeling.

(i) Our model consists in a smooth analytical mass profile, to which we add a small perturber using the `Lenstool` software (Kneib et al. 1993; Jullo et al. 2007). The main component of the model is a singular isothermal ellipsoid (SIE) with an additional contribution of an external shear. The parameters to be fitted are the SIE position, its velocity dispersion, and the external shear strength and direction. The observational constraints are the positions of the quasar images available from the HST images (Table 1). In addition, we use the ellipticity measured as a prior for the ellipticity of our mass model, i.e., we choose the SIE ellipticity to be lower than 0.1. This also implies that the model depends only weakly on the exact value of the ellipticity and PA. A flat prior is also given on the SIE position, using the astrometric error bars of Table 1. No priors are used for the other parameters. The best fit leads to $\chi^2 = 0.02$ and is obtained for an SIE with $\sigma_{\rm lens} = 215\ {\rm km\ s^{-1}}$, which converts into a total mass $M_{\rm lens} = 1.55 \times 10^{11}\ M_\odot$. The external shear is moderate, $\gamma = 0.02$, with a position angle $\theta_\gamma = 78°$. A simple smooth model therefore accounts well for the astrometry of the quasar images, as also found by previous studies. However, the predicted flux ratio between the quasar images (not included in the χ^2 calculation) are not reproduced well at all.
We then add a perturber to the overall mass potential. We describe it as a singular isothermal sphere (SIS) at the position of Object L. This adds extra free parameters to the models. In order to keep at least one degree of freedom in the fit, we successively fix the position of the lens galaxy to 25 different values within its astrometric uncertainty, and repeat the modeling. The remaining free parameters are the SIE and SIS velocity dispersions, the SIS position, and the strength of the external shear, i.e., we have five free parameters vs. six observational constraints provided by the astrometry of the quasar images.
We then adopt flat priors on the SIS position using the astrometric error bars of Object L given in Table 1. The best fit has $\chi^2 = 5.4$. The corresponding velocity dispersion for Object L is $\sigma_{\rm L} = 0.3^{+4.0}_{-0.3}\ {\rm km\ s^{-1}}$ (1-σ error bar), which translates into a mass of $M_{\rm L} < 2 \times 10^5\ M_\odot$ (1-σ). The velocity dispersion of the main lens is unchanged and the external shear is affected very little by the perturber, $\gamma = 0.018$. The mass we find for the perturber translates in a total mass-to-light ratio lower than unity in all bands. If we take the 3-σ error bar on the velocity dispersion of the SIS as an upper limit the mass-to-light ratio of Object L is barely equal to unity. It is therefore unlikely that Object L is a satellite galaxy or even a globular cluster within the halo of the lens galaxy.
In addition, we note that introducing a perturber in the model at the position of Object L does not reconcile the astrometry of the quasar images and the observed flux ratio between quasar images A, D, and C as given in Table 2 in Eigenbrod et al. (2006). Adding more mass in Object L degrades the χ^2 of the fit i.e., it affects the astrometry and still does not allow the A/D flux to be reproduced.

(ii) An alternative interpretation is that Object L is the fifth central image of the quasar, like in Winn et al. (2004). Such a central image is produced when the mass profile of the lens galaxy is very shallow or truncated in its center. We describe this feature by introducing a core radius in our SIE model, but we fail to predict a central image at the position of Object L regardless of the size of the core radius. The hypothesis of a central image can therefore safely be ruled out.

(iii) If Object L is the image of a source at the redshift of the quasar, we should see its counter image somewhere south of quasar image B and this counter image should in principle be brighter than Object L. We do not see any evidence of a counter image in the PSF-subtracted AO data or in the deconvolved HST data. Object L is most probably at a redshift different from that of the quasar. If it is at a lower redshift than the quasar, we might see it in absorption in the quasar spectrum. None of the spectra available to us (i.e., SDSS[2] and VLT from Eigenbrod et al. 2006) show any trace of absorption lines at a different redshift than that of the lens galaxy. In addition, the very deep VLT spectrum of the lens galaxy includes Object L in the slit and does not show any sign of objects at multiple redshifts. We therefore conclude that there is no evidence that Object L is at a redshift different than that of the lens galaxy and that there is no evidence that Object L is lensed.

(iv) The last simple explanation is that Object L is part of the lens galaxy but that it does not affect the lensing models much. In the deconvolved ACS image, we detect a faint feature almost aligned with Object L and the core of the lens galaxy. This feature, labeled "#4" in Fig. 4, and Object L may reflect the presence of a bar in the lens galaxy. This is also supported by our need of a disk component to model the light profile of the lens galaxy, both in the optical and in the near-IR.

6. Conclusions

Motivated by the fact that lensed quasars with anomalous flux ratios can be the signature of massive substructures in the lens galaxy, we have carried out deep VLT/AO imaging of SDSS J0924+0219, the quadruply imaged quasar with the most anomalous flux ratios known to date.

With a total of 1.35 hours of exposure in the H-band and 1.4 h in the Ks-band using the VLT NACO system and the Laser Guide Star facility, we discovered a luminous object ∼0.3″ to

[2] Available at: http://cas.sdss.org/dr7/en/tools/explore/obj.asp?ra=09:24:55.79\&dec=02:19:24.90

the north of the lens galaxy. This object, that we call Object L, is also seen on archival HST/ACS images in the *F814W filter*.

We investigated the nature of Object L using a smooth SIE model for the lens galaxy with an additional SIS perturber at the same redshift and located the position of Object L. We show that such a model cannot explain the anomalous flux ratios in SDSS J0924+0219 without also affecting the astrometry of the quasar images. The parameters found for Object L that allow a good fit of the astrometry all yield total mass-to-light ratios that are lower than or barely equal to unity.

We find evidence in the HST ACS/F814W images that Object L could be part of a bar in the lensing galaxy, oriented about along the north-south axis. This is consistent with our finding that the light profile of the lens galaxy can only be modeled with a two-components distribution that includes a significant disk.

We find no compact and luminous substructure that explains the flux ratio anomaly in SDSS J0924+0219. However the time scale of the anomaly is very large (7 years at least). Therefore it seems difficult to explain it only with microlensing. A combination of millilensing and micro-lensing is the most likely interpretation for the observations. Observations of this system from UV to mid-IR and, such as in (Fadely & Keeton 2011), would probably allow to conclude about the origin of the flux anomaly in SDSS J0924+0219.

Acknowledgements. We acknowledge T. Broadhurst and S. Suyu for useful discussions. This work is partly supported by the Swiss National Science Foundation (SNSF). D.S. acknowledges partial support from the German Virtual Observatory and from the Deutsche Forschungsgemeinschaft, reference SL172/1-1. D.S. thanks EPFL for financial support during his visit at the Laboratoire d'astrophysique where this work was finalized.

References

Auger, M. W., Treu, T., Bolton, A. S., et al. 2010, ApJ, 724, 511
Barnabè, M., Czoske, O., Koopmans, L. V. E., Treu, T., & Bolton, A. S. 2011, MNRAS, 415, 2215
Bate, N. F., Floyd, D. J. E., Webster, R. L., & Wyithe, J. S. B. 2011, ApJ, 731, 71
Biggs, A. D., Browne, I. W. A., Jackson, N. J., et al. 2004, MNRAS, 350, 949
Chantry, V., Sluse, D., & Magain, P. 2010, A&A, 522, A95
Coe, D., & Moustakas, L. A. 2009, ApJ, 706, 45
Eigenbrod, A., Courbin, F., Dye, S., et al. 2006, A&A, 451, 747
Esslinger, O., & Edmunds, M. G. 1998, A&AS, 129, 617
Fadely, R., & Keeton, C. R. 2011, AJ, 141, 101
Faure, C., Anguita, T., Alloin, D., et al. 2011, A&A, 529, A72
Fedeli, C., & Bartelmann, M. 2007, A&A, 461, 49
Fedeli, C., Bartelmann, M., Meneghetti, M., & Moscardini, L. 2008, A&A, 486, 35
Inada, N., Becker, R. H., Burles, S., et al. 2003, AJ, 126, 666
Jullo, E., Kneib, J.-P., Limousin, M., et al. 2007, New J. Phys., 9, 447
Keeton, C. R., Gaudi, B. S., & Petters, A. O. 2003, ApJ, 598, 138
Keeton, C. R., Burles, S., Schechter, P. L., & Wambsganss, J. 2006, ApJ, 639, 1
Kneib, J. P., Mellier, Y., Fort, B., & Mathez, G. 1993, A&A, 273, 367
Kochanek, C. S., & Dalal, N. 2004, ApJ, 610, 69
Koekemoer, A. M., Fruchter, A. S., Hook, R. N., & Hack, W. 2002, in The 2002 HST Calibration Workshop: Hubble after the Installation of the ACS and the NICMOS Cooling System, ed. S. Arribas, A. Koekemoer, & B. Whitmore, 337
Koopmans, L. V. E., Garrett, M. A., Blandford, R. D., et al. 2002, MNRAS, 334, 39
Koopmans, L. V. E., Treu, T., Bolton, A. S., Burles, S., & Moustakas, L. A. 2006, ApJ, 649, 599
Lombardi, G., Mason, E., Lidman, C., Jaunsen, A. O., & Smette, A. 2011, A&A, 528, A43
Magain, P., Courbin, F., & Sohy, S. 1998, ApJ, 494, 472
Mao, S., & Schneider, P. 1998, MNRAS, 295, 587
McKean, J. P., Koopmans, L. V. E., Flack, C. E., et al. 2007, MNRAS, 378, 109
Mediavilla, E., Muñoz, J. A., Falco, E., et al. 2009, ApJ, 706, 1451
Metcalf, R. B., & Zhao, H. 2002, ApJ, 567, L5
More, A., McKean, J. P., More, S., et al. 2009, MNRAS, 394, 174
Morgan, C. W., Kochanek, C. S., Morgan, N. D., & Falco, E. E. 2006, ApJ, 647, 874
Mosquera, A. M., & Kochanek, C. S. 2011, ApJ, 738, 96
Peng, C. Y., Ho, L. C., Impey, C. D., & Rix, H. 2002, AJ, 124, 266
Peng, C. Y., Ho, L. C., Impey, C. D., & Rix, H. 2010, AJ, 139, 2097
Ruff, A. J., Gavazzi, R., Marshall, P. J., et al. 2011, ApJ, 727, 96
Schechter, P. L., & Wambsganss, J. 2002, ApJ, 580, 685
Sluse, D., Courbin, F., Eigenbrod, A., & Meylan, G. 2008, A&A, 492, L39
Suyu, S. H., & Halkola, A. 2010, A&A, 524, A94
Suyu, S. H., Marshall, P. J., Auger, M. W., et al. 2010, ApJ, 711, 201
Tortora, C., Napolitano, N. R., Romanowsky, A. J., & Jetzer, P. 2010, ApJ, 721, L1
Vegetti, S., Czoske, O., & Koopmans, L. V. E. 2010a, MNRAS, 407, 225
Vegetti, S., Koopmans, L. V. E., Bolton, A., Treu, T., & Gavazzi, R. 2010b, MNRAS, 408, 1969
Winn, J. N., Rusin, D., & Kochanek, C. S. 2004, Nature, 427, 613
Yoo, J., Kochanek, C. S., Falco, E. E., & McLeod, B. A. 2005, ApJ, 626, 51
York, D. G., Adelman, J., Anderson, Jr., J. E., et al. 2000, AJ, 120, 1579